Computational and experimental analysis of flow velocity and complex vortex formation around a group of bridge piers

Water Science and Engineering 2025, 18(2): 247–258

Available online at www.sciencedirect.com

Water Science and Engineering

journal homepage: wse.hhu.edu.cn

Computational and experimental analysis of flow velocity and complex vortex formation around a group of bridge piers

Nima Ikani [a], Jaan H. Pu [a,*], Prashanth Reddy Hanmaiahgari [b], Bimlesh Kumar [c], Ebrahim Hamid Hussein Al-Qadami [d], Mohd Adib Mohammad Razi [d], Shu-yan Zang [e]

[a] *Faculty of Engineering and Digital Technologies, University of Bradford, Bradford BD7 1DP, UK*
[b] *Department of Civil Engineering, Indian Institute of Technology Kharagpur, Kharagpur 721302, India*
[c] *Department of Civil Engineering, Indian Institute of Technology Guwahati, Guwahati 781039, India*
[d] *Faculty of Civil Engineering and Built Environment, University of Tun Hussein Onn, Parit Raja 86400, Batu Pahat, Johor, Malaysia*
[e] *Shenyang University of Chemical Technology, Shenyang 110142, China*

Received 29 July 2024; accepted 9 December 2024
Available online 27 January 2025

Abstract

In this study, the flow characteristics around a group of three piers arranged in tandem were investigated both numerically and experimentally. The simulation utilised the volume of fluid (VOF) model in conjunction with the $k-\varepsilon$ method (i.e., for flow turbulence representations), implemented through the ANSYS FLUENT software, to model the free-surface flow. The simulation results were validated against laboratory measurements obtained using an acoustic Doppler velocimeter. The comparative analysis revealed discrepancies between the simulated and measured maximum velocities within the investigated flow field. However, the numerical results demonstrated a distinct vortex-induced flow pattern following the first pier and throughout the vicinity of the entire pier group, which aligned reasonably well with experimental data. In the heavily narrowed spaces between the piers, simulated velocity profiles were overestimated in the free-surface region and underestimated in the areas near the bed to the mid-stream when compared to measurements. These discrepancies diminished away from the regions with intense vortices, indicating that the employed model was capable of simulating relatively less disturbed flow turbulence. Furthermore, velocity results from both simulations and measurements were compared based on velocity distributions at three different depth ratios (0.15, 0.40, and 0.62) to assess vortex characteristic around the piers. This comparison revealed consistent results between experimental and simulated data. This research contributes to a deeper understanding of flow dynamics around complex interactive pier systems, which is critical for designing stable and sustainable hydraulic structures. Furthermore, the insights gained from this study provide valuable information for engineers aiming to develop effective strategies for controlling scour and minimizing destructive vortex effects, thereby guiding the design and maintenance of sustainable infrastructure.

Keywords: CFD computation; ADV measurements; Pier group; Flow turbulence; Velocity profile

1. Introduction

Bridge pier structures pose significant challenges to aquatic environments due to their tendency to exacerbate scouring in their vicinity (Lade et al., 2019). Alluvial channel features and scour surrounding bridge piers are critical areas of study that require further research to enhance our understanding (Chavan and Kumar, 2017; Chavan et al., 2020). Long-term flow repercussion can lead to bridge failure, thereby attracting considerable attention from various studies (Dargahi, 1989; Hong et al., 2012; Prendergast and Gavin, 2014; Loli et al., 2022; Soori and Karami, 2024). In academic research, numerical models are frequently used to simulate flow hydrodynamics, complementing laboratory experiments conducted around bridge piers (Alemi et al., 2019; Zaid et al., 2019). For

* Corresponding author.
E-mail address: J.H.Pu1@bradford.ac.uk (Jaan H. Pu).
Peer review under responsibility of Hohai University.

https://doi.org/10.1016/j.wse.2025.01.003

instance, numerous studies have been conducted to determine turbulent mean velocity profiles and develop hydrodynamic computational fluid dynamics (CFD) models to achieve accurate velocity distributions (Salaheldin et al., 2004; Jia et al., 2018; Pourshahbaz et al., 2022). These efforts aim to enhance our understanding of flow behaviour, ultimately providing more reliable assessments of bridge pier performance over time.

Due to the complexity of three-dimensional (3D) turbulent flow, advanced modelling techniques and computational resources are essential for accurately simulating and analysing flow behaviour around bridge piers (Helmi and Shehata, 2021). Numerous studies have focused on the flow field around a single pier using various CFD models (Huang et al., 2009; Ghaderi and Abbasi, 2019). These studies have conducted simulations using 3D CFD models to examine scale effects on turbulent flow. However, fewer attempts have been made to utilise CFD for modelling the flow induced by two or three piers, primarily due to the inherent complexity of such scenarios (Bao et al., 2010; Hamidi and Siadatmousavi, 2018; Qi et al., 2020; Ataie-Ashtiani and Aslani-Kordkandi, 2012). Recent advancements in CFD have led to the development of multi-scale turbulence models that can effectively calculate the turbulent kinetic energy (TKE) spectral distribution (Pedras and de Lemos, 2000). These models hold promise in addressing the challenges posed by the scale and gradient of TKE in turbulent flows around multiple bridge piers.

There have been relatively few studies conducted to simulate flow near bridge piers and related it to turbulence behaviour. One relevant study by Salaheldin et al. (2004) employed CFD to investigate the effects of various turbulence models on simulating the 3D separated vortical flow field around a single bridge pier in clear water. They examined the distribution of velocity, flow patterns, and the effect of a flatbed on flow behaviour. Their findings indicated that both the standard and Renormalization Group (RNG) $k-\varepsilon$ models effectively computed the flow field around the pier, although both turbulence models slightly overestimated the velocity near the bed. Furthermore, Huang et al. (2009) investigated the impact of scale effects on turbulent flow and sediment scour using a 3D CFD model. An experimental model of scour around a small-scale bridge pier was also used to validate the data obtained from the proposed CFD model, which incorporated a two-equation turbulence model. In their study, the qualitative flow patterns predicted by the FLUENT model exhibited satisfactory agreement with experimental observations, despite the complexity of the phenomena involved.

In the past two decades, acoustic Doppler velocimetry (ADV) has been extensively studied due to its reasonable accuracy in measuring 3D flow velocities and relevant fluctuations (Song and Chiew, 2001; Hu and Yu, 2023)). However, this technique has some limitations. Although ADV systems are user-friendly, they are intrusive and can produce unavoidable noise, leading to poor measurement conditions (Park and Hwang, 2021). Despite advancements in ADV technology, there remains room for improvement in measuring flow turbulence. Studies have demonstrated enhancements of ADV in sampling methods, post-processing of velocity data, and noise reduction techniques to improve measurement accuracy (Li et al., 2007; Marian et al., 2021; Díaz Lozada et al., 2021). The capability of three-receiver ADV systems to measure 3D flow fields has been explored. However, these systems often encounter noise signals that compromise turbulence measurements (Blanckaert and Lemmin, 2006). By incorporating a fourth receiver and optimizing transducer settings, it is possible to significantly reduce noise, thereby expanding the sampling frequency range.

Voulgaris and Trowbridge (1998) evaluated the accuracy of ADV in a 17-m flume and compared it to a laser Doppler velocimeter (LDV). Measurements confirmed that ADV can accurately measure mean velocities within a discrepancy of 1% compared to reference values, up to a distance less than 1 cm from the boundary. However, deviations were observed closer to the boundary, attributed to the ADV's sample volume size. Further investigations into capturing 3D turbulent flows revealed operational complexities that affect ADV's accuracy (Park and Hwang, 2021). A refined measurement strategy with a four-receiver ADV system demonstrated significant noise reduction and highlighted the need for a lower sampling period. As a result of these proven improvements, a four-receiver ADV system was utilised in this study to obtain reliable flow and turbulence measurements.

This study aimed to numerically and experimentally investigate the flow characteristics induced by a complex group of bridge piers using the ANSYS FLUENT model and ADV measurements. This study examined the details of reversal flow velocity and vortex dynamic features around multiple bridge piers at varying flow depths, an area that has received limited attention in previous studies. While many researchers have focused on flow fields around individual piers or different pier shapes, this study uniquely combined experimental and numerical approaches to analyse the complex flow behaviours specifically associated with multiple piers in close vicinity. Numerically, a second-order characteristic-based $k-\varepsilon$ method was used to analyse the 3D flow behaviour and vortices around a complex group of three square bridge piers arranged in tandem. The numerical results were compared with measurements conducted in an experimental flume under transient flow conditions, focusing on flow velocity. The findings indicated that the numerical results aligned well with the measured data regarding flow field characteristics and velocity distribution. Furthermore, the insights gained from this study can provide valuable information for engineers aiming to develop effective strategies for controlling scour and minimizing destructive vortex effects. This research contributes to a deeper understanding of flow dynamics around complex interactive pier systems, thereby guiding their design and maintenance for sustainable infrastructure.

2. Methods

2.1. Numerical model details

In this study, the Navier−Stokes (NS) equations, which govern fluid flow, were solved using the volume of fluid (VOF)

model fully coupled with k–ε equations. To enhance the accuracy and reliability of the model, particular attention was given to geometry and mesh sensitivity analyses. As the simulations progressed, the residual errors associated with these equations gradually decreased, indicating convergence and stability of the numerical solution.

2.1.1. Governing equations

The governing 3D CFD approach can be expressed through the continuity equation (Eq. (1)) and the momentum equations (Eqs. (2) through (4)), which represent the conservation of mass and momentum in a fluid domain (Pu et al., 2007, 2012):

$$\frac{\partial \rho}{\partial t}+\frac{\partial(\rho u)}{\partial x}+\frac{\partial(\rho v)}{\partial y}+\frac{\partial(\rho w)}{\partial z}=0 \tag{1}$$

$$\frac{\partial(\rho u)}{\partial t}+\nabla\cdot(\rho u\boldsymbol{V})=-\frac{\partial P}{\partial x}+\frac{\partial \tau_{xx}}{\partial x}+\frac{\partial \tau_{yx}}{\partial y}+\frac{\partial \tau_{zx}}{\partial z}+\rho f_x \tag{2}$$

$$\frac{\partial(\rho v)}{\partial t}+\nabla\cdot(\rho v\boldsymbol{V})=-\frac{\partial P}{\partial y}+\frac{\partial \tau_{xy}}{\partial x}+\frac{\partial \tau_{yy}}{\partial y}+\frac{\partial \tau_{zy}}{\partial z}+\rho f_y \tag{3}$$

$$\frac{\partial(\rho w)}{\partial t}+\nabla\cdot(\rho w\boldsymbol{V})=-\frac{\partial P}{\partial z}+\frac{\partial \tau_{xz}}{\partial x}+\frac{\partial \tau_{yz}}{\partial y}+\frac{\partial \tau_{zz}}{\partial z}+\rho f_z \tag{4}$$

where ρ is the fluid density; t is the time; u, v, and w are the velocity components in the x, y, and z directions, respectively; $\boldsymbol{V}$ is the velocity vector; P is the pressure; τ_{xx}, τ_{yy}, and τ_{zz} are the normal stresses caused by viscosity in the x, y, and z directions, respectively; τ_{yx}, τ_{zx}, τ_{xy}, τ_{zy}, τ_{xz}, and τ_{yz} are the shear stresses describing how motion in one direction influences stress in another direction; and f_x, f_y, and f_z are the body force components per unit volume in the x, y, and z directions, respectively.

The momentum equations describe the conservation of momentum in the x, y, and z directions. In Eqs. (2) through (4), the terms, $\partial(\rho u)/\partial t$, $\partial(\rho v)/\partial t$, and $\partial(\rho w)/\partial t$, represent the rate of momentum changes over time in each corresponding direction. The expressions, $\nabla\cdot(\rho u\boldsymbol{V})$, $\nabla\cdot(\rho v\boldsymbol{V})$, and $\nabla\cdot(\rho w\boldsymbol{V})$, account for the convection of momentum due to the fluid's movement in space. The gradients of the pressure (P), including $\partial P/\partial x$, $\partial P/\partial y$, and $\partial P/\partial z$, describe how pressure forces drive fluid motion in their respective directions. The terms, ρf_x, ρf_y, and ρf_z, represent external body forces, such as gravity, acting on the fluid in the x, y, and z directions, respectively.

To capture the complexities of turbulence, the k–ε model introduces two additional transport equations for kinetic energy (k) (Eq. (5)), which represents the TKE in this study, and turbulent dissipation rate (ε) (Eq. (6), which enhances the accuracy of predictions in complex turbulent flows (Pu et al., 2014):

$$\frac{\partial(\rho k)}{\partial t}+\nabla\cdot(\rho k\boldsymbol{V})=\nabla\cdot\left[\left(\mu+\frac{\mu_t}{\sigma_k}\right)\nabla k\right]+P_k-\rho\varepsilon \tag{5}$$

$$\frac{\partial(\rho\varepsilon)}{\partial t}+\nabla\cdot(\rho\varepsilon\boldsymbol{V})=\nabla\cdot\left[\left(\mu+\frac{\mu_t}{\sigma_\varepsilon}\right)\nabla\varepsilon\right]+\frac{C_{1\varepsilon}\varepsilon(G_k+C_{3\varepsilon}G_b)}{k}-\frac{C_{2\varepsilon}\rho\varepsilon^2}{k} \tag{6}$$

where μ is the molecular viscosity; μ_t is the turbulent viscosity; σ_k is the turbulent Prandtl number for k; P_k is the production of TKE due to velocity gradients; σ_ε is the turbulent Prandtl number for ε; $C_{1\varepsilon}$, $C_{2\varepsilon}$, and $C_{3\varepsilon}$ are the model constants for the dissipation rate equation; G_k is the mean velocity gradient; and G_b represents the hydrodynamic effect. In Eq. (5), $\partial(\rho k)/\partial t$ represents the rate of TKE changes over time; $\rho k\boldsymbol{V}$ denotes the transport of TKE by mean flow; $(\mu+\mu_t/\sigma_k)\nabla k$ represents the diffusion of TKE; and $\rho\varepsilon$ is the dissipation rate, which is negative. In Eq. (6), $\partial(\rho\varepsilon)/\partial t$ represents the rate of changes in turbulent dissipation rate over time; $\rho\varepsilon\boldsymbol{V}$ denotes the convective transport of the dissipation rate by mean flow; $(\mu+\mu_t/\sigma_\varepsilon)\nabla\varepsilon$ corresponds to the diffusion of the dissipation rate considering both molecular and turbulent viscosity effects; $C_{1\varepsilon}\varepsilon(G_k+C_{3\varepsilon}G_b)/k$ represents the production of the dissipation rate, including the components from TKE production due to mean velocity gradients (G_k) and hydrodynamic effects (G_b) determined by model constants ($C_{1\varepsilon}$ and $C_{3\varepsilon}$); and $C_{2\varepsilon}\rho\varepsilon^2/k$ describes how TKE is dissipated into heat, acting as a sink in energy balance.

In this study, pressure correction in simulations was performed using the semi-implicit method for pressure-linked equations (SIMPLE), while a second-order scheme was applied for temporal discretisation. This technique facilitates the design of a free water surface by coupling the cells throughout the domain, excluding those near the surface. It also enables a detailed investigation of flow characteristics, including the formation and behaviour of variations in the water surface. Importantly, no numerical instabilities were observed in the simulations, particularly in turbulent channel flow predictions that employed smooth boundary conditions and a complex grid structure in all directions. An implicit second-order scheme was implemented for temporal discretisation.

2.1.2. Modelling and geometry

Flow characteristics exhibit significant variability due to the presence of different types of piers and variations in channel bed geometry (Melville and Raudkivi, 1996; Yang et al., 2021). Slight changes in channel geometry can result in drastic flow turbulence in multiple dimensions (Pu, 2015). The geometric configuration and smooth boundary conditions for numerical simulations are illustrated in Fig. 1(a), where a flow domain length of 1.35 m was considered to facilitate meaningful comparisons between numerical simulations and experimental observations. To ensure effective operation of this flow domain within the numerical model, inflow and outflow boundaries were designated as open and transmissive, while the pier-block and sidewall surfaces were assigned as solid boundaries.

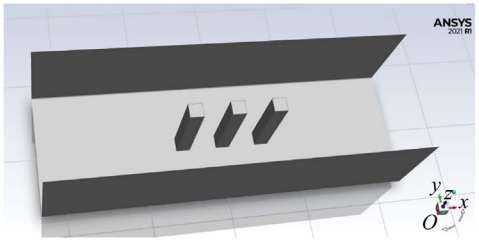

(a) Geometric setup and smooth boundary conditions for bridge pier group in 3D modelling domain

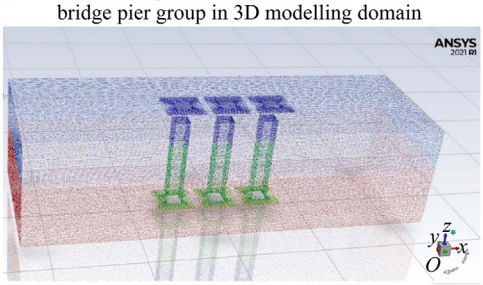

(b) Domain area in VOF model of ANSYS FLUENT

Fig. 1. Geometric setup and smooth boundary conditions for bridge pier group in 3D modelling domain and domain area in VOF model of ANSYS FLUENT.

As illustrated in Fig. 1(b), the VOF model, a well-established multiphase flow computational approach, was employed to analyse a two-phase domain in which water flows in a channel with an upper region occupied by air. Various VOF models are commonly used in 3D numerical simulations to effectively handle free surface boundaries and interactions between different phases, such as water and air. Several studies have demonstrated the effectiveness of this model (Hirt and Nichols, 1981; Ramamurthy et al., 2005; Amina and Tanaka, 2022). To ensure smooth simulation, the air-to-water depth ratio should be at least 0.5, regardless of boundary conditions at water surface (Karim et al., 2009). In this study, an air domain depth of 0.1 m was employed, maintaining the desired ratio with the water depth while preventing violations of water surface breaking or sloshing rule.

For the simulations conducted in this study, each time step consisted of 20 iterations, with a time step size of 0.005 s selected based on the finest requirements of Courant criteria. These specific parameters were chosen to ensure both accurate and stable simulations while preventing divergence. Flow problems were solved using pressure-based solvers with coupled schemes. By incorporating a pressure−velocity coupling algorithm in SIMPLE, this method serves as a suitable alternative to density-based and pressure-based separated algorithms.

2.1.3. Mesh sensitivity analysis

Meshing was conducted using hexahedral mesh elements of a standard decomposition type, resulting in a model comprising approximately 2.3 million nodes and 2.23 million elements. A multi-zone meshing approach was employed, leading to the generation of two split faces within the mesh body (Fig. 2). This method facilitated enhanced control and refinement of meshes to achieve two primary objectives: (1) to enable a more precise representation of complex flow behaviour and (2) to capture finer details of flow features. In the overall domain, a general element size of 0.005 m was utilised. However, near the piers, where flow behaviour becomes more complex, a smaller element size of 0.001 m was implemented. Resolving the thin viscous sublayer in 3D flows with high Reynolds numbers necessitates a complex grid structure, as highlighted by Ferziger et al. (2002).

To ensure numerical accuracy in CFD simulations, a grid independence study was conducted by initially testing uniform mesh sizes of 0.1 m, 0.01 m, and 0.009 m across the entire domain. The finer meshes still resulted in significant discrepancies near the piers, which could be improved by applying different mesh densities for the main body and the near-pier region. After further refinement, the optimal configuration was determined to be a mesh size of 0.005 m for the main body and 0.001 m for the area near the piers. The large mesh with a size of 0.1 m, which contained 31 830 nodes and 25 114 elements, proved insufficient for accurate results. In contrast, the medium mesh with a size of 0.01 m, with 428 652 nodes and 407 120 elements, and the finer mesh with a size of 0.009 m, with 567 368 nodes and 541 360 elements, demonstrated significantly improved accuracy.

The standard wall function suggests that the velocity distribution in the immediate vicinity of a wall is similar across various turbulent flows characterised by significant pressure gradients. A key parameter for assessing the suitability of the wall function is the dimensionless wall distance (Y^+). In this study, the height of the first layer from the bed ($h_{\text{bed}} = 0.001\,9$) was selected to accurately represent the flow near the wall region based on the following equations:

$$h_{\text{bed}} = \frac{Y^+}{U_\tau \rho} \tag{7}$$

$$U_\tau = \sqrt{\frac{0.058 R_{\text{l}}^{-0.5} U_\infty^2}{2}} \tag{8}$$

where U_τ is the friction velocity, U_∞ is the free-stream velocity (the velocity in the flow far from the wall), and R_{l} is the characteristic length (Kim et al., 1999).

Additionally, the inflation mesh technique was utilized to facilitate a smooth transition near the wall. This technique effectively captures flow gradients and ensures accurate resolution of the boundary layer, especially in the near-wall region. The side boundaries of the domain were treated as smooth sidewalls that did not significantly impact the flow field surrounding the pier.

2.2. Laboratory measurements

2.2.1. Experimental setup

During laboratory measurements, flow characteristics were observed around three square piers situated on a smooth bed.

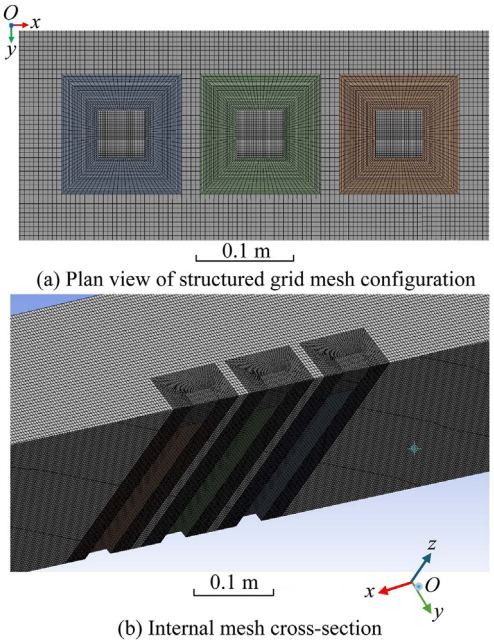

(a) Plan view of structured grid mesh configuration

(b) Internal mesh cross-section

Fig. 2. Optimized mesh grid design for accurate flow simulations around piers.

To achieve the objectives of this study, the same pier geometry and flow conditions used in the laboratory experiments were replicated in the numerical model. Experiments was conducted in a smooth-bed rectangular open channel flow flume located at the hydraulic laboratory at the University of Bradford (Fig. 3). The flume has dimensions of 12 m in length, 0.5 m in height, and 0.45 m in width. This experimental setup featured a closed-loop recirculating flume system designed for controlled flow studies. Water was pumped from a storage tank into an input tank, which then directed the flow into the channel. The channel was equipped with glass sidewalls to enhance visibility during observations and featured a smooth stainless-steel plate as the bed to ensure consistent flow dynamics. The bed slope was set at 0.003 3.

Three square piers, each with dimensions of 0.05 m × 0.05 m (plan-view surface), were positioned at a distance of $2d$ ($d = 0.05$ m) from each other. In the numerical study, a flume domain with dimensions of 1.35 m in length, 0.45 m in width, and 0.50 m in height was utilized (Fig. 4). The surface of the piers was smooth.

Flow around bridge piers exhibits complex and turbulent behaviour within the boundary layers, while transition occurs

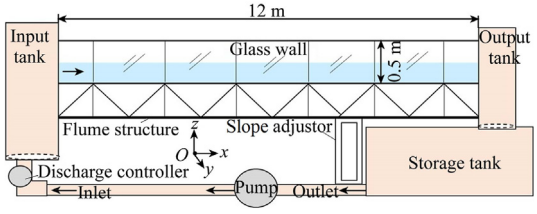

Fig. 3. Schematic diagram of experimental recirculating flume system and flume structure.

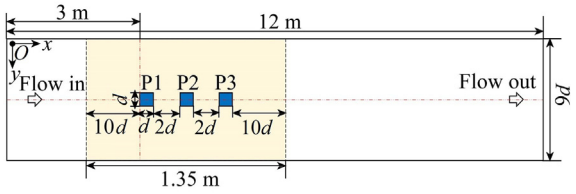

Fig. 4. Location of group of three square piers in experiments with P1, P2, and P3 denoting first, second, third piers, respectively.

in the free shear layers, as highlighted by Breuer (2000). Despite the presence of turbulence, the observed Froude number of approximately 0.5 indicated a subcritical flow condition. Due to measurement restrictions, laboratory data could not be recorded at points closer than 2.5 cm ($0.5d$) to the piers. However, compared to the experimental study, numerical analysis can provide additional insights into the flow field. A comprehensive understanding of flow characteristics was achieved by measuring velocities at 60 different locations selected based on a schematic plan (Fig. 5), allowing for a detailed analysis of flow patterns and hydrodynamics within the studied flow area.

2.2.2. Assessment of measurement uncertainty in Vectrino velocity data

Data uncertainty analysis was performed for the Vectrino measurements to verify the accuracy and reliability of the findings of this study. Prior to data collection, calibration tests were conducted four times to confirm the consistency of the velocity profiles at the same location in undisturbed conditions. The uncertainty was quantified using the standard deviation (σ) of repeated measurements. The relative uncertainty (U_r) was then calculated as $U_r = (\sigma/V_{mean}) \times 100\%$, where V_{mean} is the mean velocity. The results indicated that the relative uncertainty was 0.55%, falling within an acceptable range of errors.

2.2.3. ADV

ADV is an essential tool in hydrodynamics, capable of precisely measuring 3D flow velocities by utilizing the Doppler shift principle in fluid flows (Discetti and Coletti, 2018). To evaluate flow characteristics, velocity data were

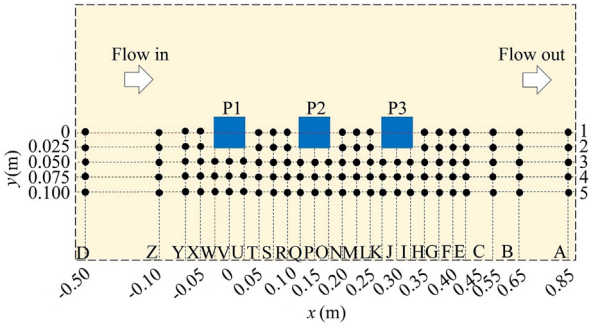

Fig. 5. Schematic plan of locations of ADV measurements in experiments.

collected using a Nortek side-looking ADV system. The instrument was strategically placed within the central cross-sectional area of the flume, located 3 m downstream of the channel entrance. Data collection involved recording velocity data at each point for a duration of 5 min, with a sampling frequency of 100 Hz.

To ensure accuracy and precision, the ADV probe realignment method proposed by Pu et al. (2014) and Pu (2021) was implemented to enhance the locational precision of the profile and improve data quality. In this study, data collection was conducted by positioning the probe at the lowest point (0.005 m) and then moving it upward between sampling rounds. This approach consistently produced data with high correlations (greater than 70%) and minimum signal-to-noise ratios (SNRs) of 15%, significantly reducing data errors. During data preprocessing, any velocity reading with a correlation value below 70% or an inadequate SNR was re-recorded. By following careful data collection and handling strategies, including advanced signal processing techniques and thorough calibration protocols, the reliability of measurements was maintained.

2.2.4. Boundary conditions

In the streamwise direction, the distance from the inlet to the first pier was set as 3 m, ensuring that the flow reached a fully developed state before encountering the piers during the experiment. A uniform upstream velocity of 0.76 m/s was achieved, with a discharge of 0.072 m^3/s and a consistent flow depth of 0.21 m recorded throughout the flume prior to the implementation of pier blocks. The measurement domain length was set as 1.35 m.

3. Results and discussion

After applying the same initial flow and boundary conditions from the experiment to the CFD model, comparisons were conducted for computational validation. Fig. 6 shows the simulated velocity field between water and air, highlighting how friction between the two fluids varied across a specified area. The figure emphasises the influence of the piers on flow patterns and the induction of turbulence. The presence of piers significantly affected flow dynamics, causing turbulence to develop and intensify. The accelerated flow around piers led to increased turbulence behind the piers, as evidenced by variations in water depth.

3.1. Flow features at horizontal planes

Fig. 7 provides a detailed visualisation of the flow characteristics around the complex group of piers, including the contour plots of velocity streamlines at the $x-y$ planes obtained from simulations conducted in both the inner ($z/h \leq 0.2$, where h is the water depth) and outer ($z/h > 0.2$) flow regions. Additionally, the contour plots of experimental streamwise velocity at the $x-y$ planes are illustrated for comparison. The plots clearly indicate that several vortices formed, particularly prevalent in the gaps between the piers. This observation

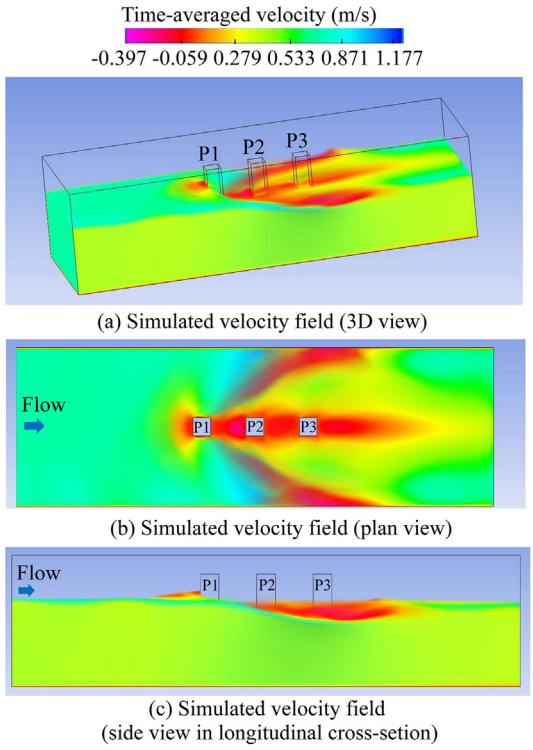

Fig. 6. Time-averaged velocity field around three square piers on a smooth bed.

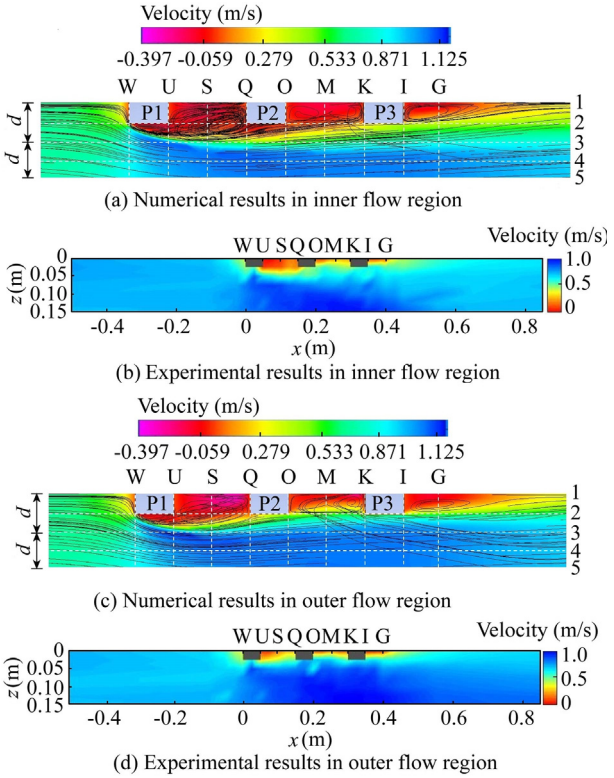

Fig. 7. Contour plots of velocity streamlines at $x-y$ planes in inner and outer flow regions from experimental measurements and numerical simulations.

aligns with the laboratory findings of Ikani et al. (2023), who conducted quadrant analysis and found a dominant sweep cycle between piers. Ikani et al. (2024) reported that the depth-averaged streamwise velocity corresponded with the interference of flow turbulence in the region between piers, contributing to the formation of strong vortices. Notably, the presence of suppressed streamlines became more pronounced as the distance from the pier wall decreased. The numerical results indicated the occurrence of circulation phenomena throughout the entire depth zone after each pier, resulting in vortex formation. As the distance from the sidewall was large, its impact on the vicinity of the piers became negligible. Therefore, flow in the sidewall region exhibited relatively smoother streamlines with minimal disturbance. These observations, derived from velocity streamline and contour plots, enhanced our understanding of the vortex formation process in the studied area. A detailed comparison with experimental data revealed slight discrepancies in simulated flow structures, particularly regarding interactions between the piers at specific locations: O3 and G1 in the inner flow region, and R3, N2, and M2 in the outer flow region. However, the general features and locations of intensive vortices were accurately simulated, underscoring a reasonable representation from the modelling strategy (i.e., coupling of 3D VOF with the $k-\varepsilon$ model).

3.2. Flow features at vertical planes

Fig. 8 shows the contour plots of the time-averaged velocity at five vertical ($x-z$) planes: $y = 0$, $0.5d$, d, $1.5d$, and $2.0d$. The vertical plane at $y = 0$ serves as the symmetry plane, while the plane at $y = 0.5d$ includes all piers along the x axis. The velocity contour plots indicate that flow velocity decreased as the flow approached the first pier, followed by an acceleration around the second pier. In the wake region near the piers, flow separation occurred, resulting in the formation of a reverse flow region. According to numerical simulations, the peak velocity in the wake zone behind the first pier was approximately −0.20 m/s, which aligned reasonably well with the experimental value of −0.25 m/s. This finding indicated that the numerical model effectively simulated flow wake dynamics.

A detailed analysis of the contour plots across various planes further revealed complex fluid dynamics in the vicinity of the piers. At the symmetry plane ($y = 0$), the flow velocity distribution remained relatively uniform until encountering the first pier, where significant deceleration occurred due to obstruction. This deceleration highlighted boundary layer effects and adverse pressure gradients that contributed to an increase in TKE near the pier. As the flow reached the second pier, acceleration was observed, characterised by narrower velocity contours and an increase in velocity magnitude. This acceleration suggested enhanced shear Reynolds stresses, a sign of vortex formation and flow instability. The interaction between the piers further amplified these effects, particularly in the pier gap regions.

At planes at $y = d$ and beyond, flow dynamics were dominated by the wake region formed behind the first pier. The contour plots at these planes reveal a large separation

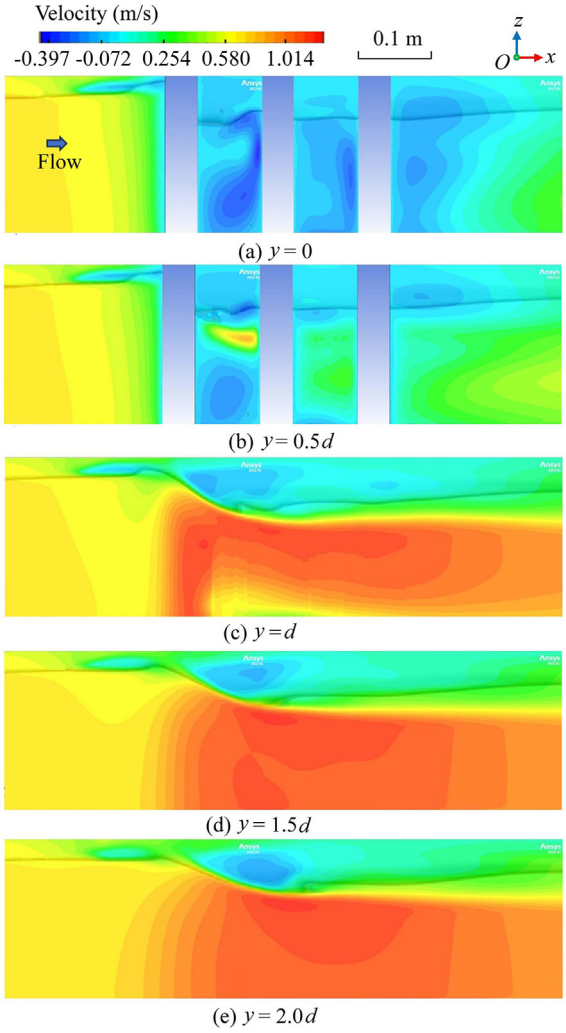

Fig. 8. Contour plots of flow velocity from numerical simulations at five vertical ($x-z$) planes ($y = 0$, $0.5d$, d, $1.5d$, and $2.0d$).

region with a significant reverse flow, where velocity magnitude peaked at approximately −0.2 m/s. This reverse flow region clearly indicated a highly turbulent wake, where flow transitioned from a more organised structure upstream to a chaotic and energy-dissipative regime downstream. Due to the interaction between shed vortices and free-stream flow, turbulence intensity remained elevated in this region. As flow continued past planes at $y = 1.5d$ and $y = 2.0d$, recirculation zones persisted, although their intensity gradually diminished.

The vector plots derived from the streamwise velocity component in the simulation (Fig. 9) indicate that the piers caused deflection of the approaching flow in the vertical direction. Five different vertical planes were designed with gaps to demonstrate the locations of vertically mounted piers. Due to the small space between the piers, a reverse flow region was visible behind each pier, exhibiting nearly non-varying depths after the first pier (refer to the air−water interface in the plots). In front of each pier, the approaching flow was directed towards the pier and then deflected back, resulting in the formation of vortices primarily near the pier wall. Alongside the piers, a reverse flow region was observed due to flow

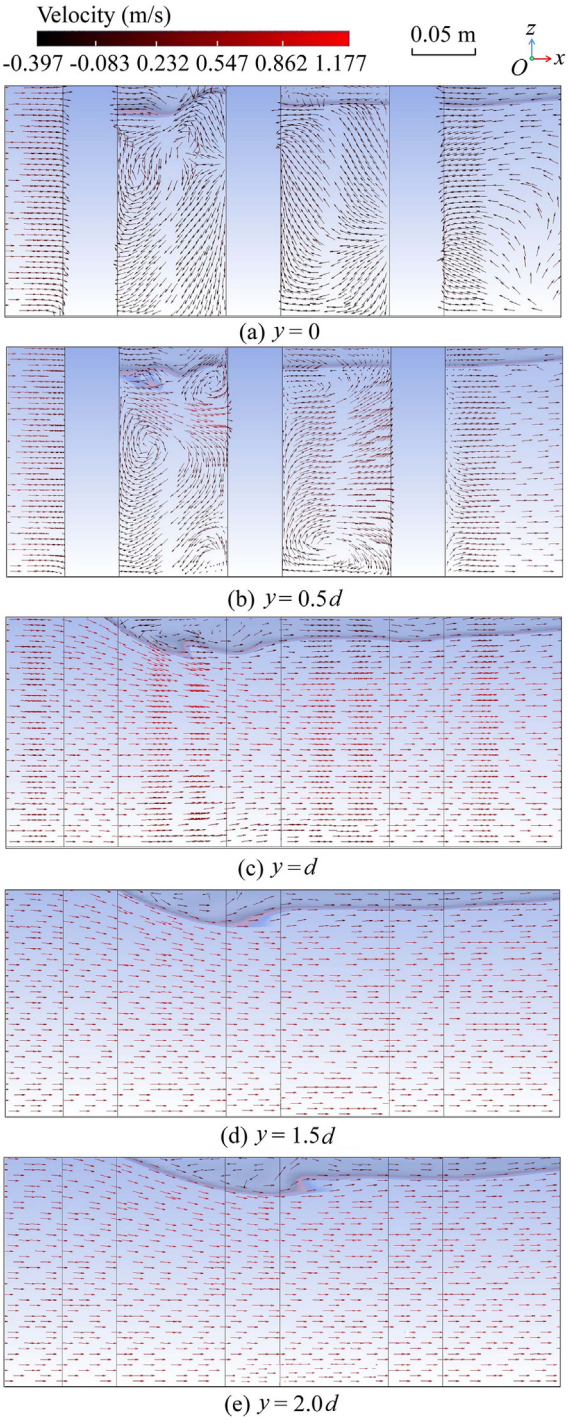

Fig. 9. Time-averaged two-dimensional velocity vector at five vertical planes (y = 0, 0.5d, d, 1.5d, and 2.0d).

separation. The reversal velocity after the first pier indicated the presence of vortex structures, which significantly influenced flow dynamics. These vortex structures exhibited a gradual decrease in strength from upstream to downstream. Additionally, there was a stronger downward flow than an upward flow after the first pier (in the gap between the first and second piers), attributed to the vortex formed after the first pier. This vortex created a significant downward pressure gradient that pulled flow downwards more strongly than it pushed upwards, a phenomenon also suggested by Ikani et al. (2023). From the bed to the flow surface, the longitudinal length of these vortex structures decreased. However, after the last pier, this length increased across the flow depth.

3.3. Comparison of flow features on horizontal planes

Fig. 10 shows the experimental velocity at depth ratios (z/h) of 0.15, 0.40, and 0.62. The phenomenon of reversal velocity occurring after the piers was clearly observed, confirming the model's accuracy in capturing the behaviour of vortex-intensive flows using the simplified turbulent $k-\varepsilon$ approach. This was supported by the simulated results at the same z/h ratios (Fig. 11). The model successfully reproduced the phenomenon of reversal velocity with reasonable magnitudes, demonstrating its capability to capture key flow characteristics in complex flow scenarios.

As shown in Fig. 11, the simulated velocity vectors indicated circulation and reverse flow near the piers, particularly at z/h = 0.15. The reverse flow created wake vortices between the piers, with evident separation zones behind each pier. These separation zones extended further downstream at higher z/h levels of 0.40 and 0.62, demonstrating how the wake structure varied with depth. Additionally, the rapid recovery of the vortex-induced flow after the third pier indicated a complex dynamic interaction between the vortices and flow, leading to faster stabilisation of the flow field in this region.

Furthermore, the velocity vector field demonstrated lateral changes in flow directions at three different depth levels, caused by the flow colliding with the piers. This phenomenon distinctly highlights the involvement of transverse flow in the creation of vortices, as supported by Ikani et al. (2023).

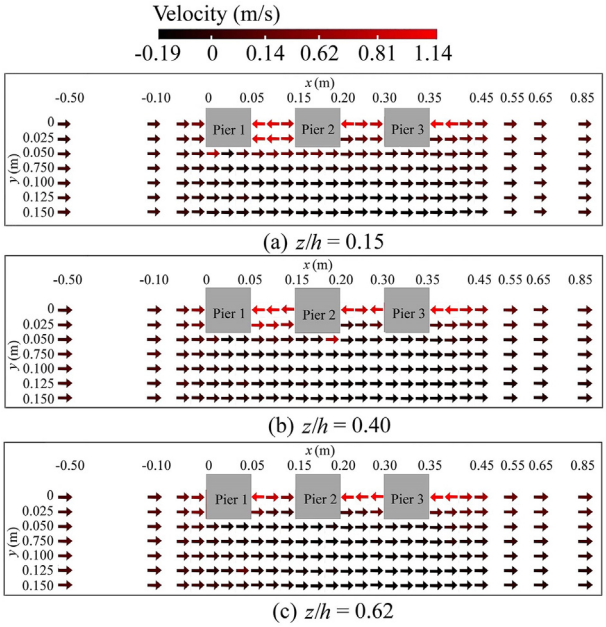

Fig. 10. Velocity distributions derived from experiments at $x-y$ planes (z/h = 0.15, 0.40, and 0.62).

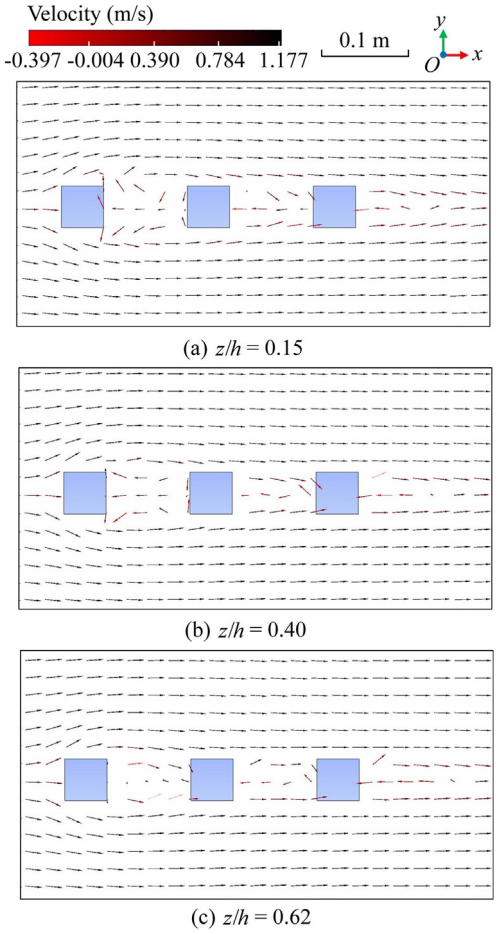

Fig. 11. Velocity distributions derived from numerical simulations at $x-y$ planes (z/h = 0.15, 0.40, and 0.62).

3.4. Comparison of streamwise velocity profiles

Fig. 12 presents a detailed comparison of velocity profiles at various distances from the piers across different positions. The figure is organised to illustrate both vertical and horizontal variations in flow behaviour, providing evidence of where the numerical model aligned well with the experimental data and where discrepancies occurred, particularly around the piers. Both the experimental data and numerical results showed decelerated flow as it approached the initial pier. However, significant deviations in velocity were observed, particularly near the piers and in the gap regions between them. These discrepancies highlighted the challenges in modelling flow turbulence under complex pier configurations, particularly near the water surface.

The alignment between numerical and experimental profiles was notably strong in both upstream and downstream sections, as well as further away from the piers, indicating the efficacy of the model for simulating flow behaviour in these regions. However, a notable discrepancy in velocity profiles emerged between the piers, where the numerical results diverged from the observations. This discrepancy is typically caused by the complexity of flow behaviour, including intricate vortices and real-world phenomena that are challenging to simulate accurately. At y = 0 m, the numerical results closely aligned with the experimental data for the first and second piers, with deviations within a range of 5%−10%. For instance, at x = −0.05 m, the velocity profile showed a deviation less than 5%, indicating good agreement in less turbulent areas. However, near the third pier, particularly around the pier, the discrepancies increased significantly, with deviations reaching 15%−20%, as observed at x = 0.275 m. At y = 0.025 m and y = 0.050 m, the numerical results exhibited even larger discrepancies, especially near the piers and closer to the water surface, where deviations reached up to 25%−30%. These discrepancies were attributed to the formation of large-scale eddies near the surface, demonstrating the limitations of the $k-\varepsilon$ model in accurately reproducing flow turbulence in this specific context compared to the computationally expensive models like the large eddy simulation (LES), as suggested by simulations in Cheng et al. (2003). Despite these discrepancies, all key velocity distribution features, particularly in undisturbed regions, recovery areas, and sidewall regions, were accurately simulated. This validation confirmed the reliability of the proposed CFD model in capturing complex flow dynamics around a group of piers.

4. Conclusions

This study investigated flow dynamics induced by a group of three piers through computational and experimental methods. The assessment of the flow field revealed a distinct separation zone located behind the first pier, characterised by its downstream extension closer to the free surface. This phenomenon was primarily driven by the development of a downward flow induced by the negative pressure gradient resulting from non-uniform approaching flow near the sides of the piers. The interaction between this downward flow and the separation of horizontal boundary layer near the bed contributed to the formation of vortices and the emergence of a dynamically evolving complex flow pattern behind each pier. The ability of the numerical model to simulate measured turbulence behaviour and vortex formation, especially in regions around the piers where high vortex intensity was recorded, was evaluated. The simulated velocity distributions and flow field contour maps were validated against experimental measurements, demonstrating reasonable correspondence and confirming the efficacy of the coupled modelling approach. Despite some limitations in representing flow turbulence, the $k-\varepsilon$ model showed significant potential as a practical tool for computing flow turbulence for complex flow applications.

Furthermore, applying the discussed measurement techniques to real-world bridge piers presents practical challenges due to the complex nature of field conditions, including variable flow rates, sediment deposition, and logistical difficulties associated with instrument implantation around large-scale structures. Nevertheless, the findings of this study contribute to a better understanding of flow behaviour and critical flow

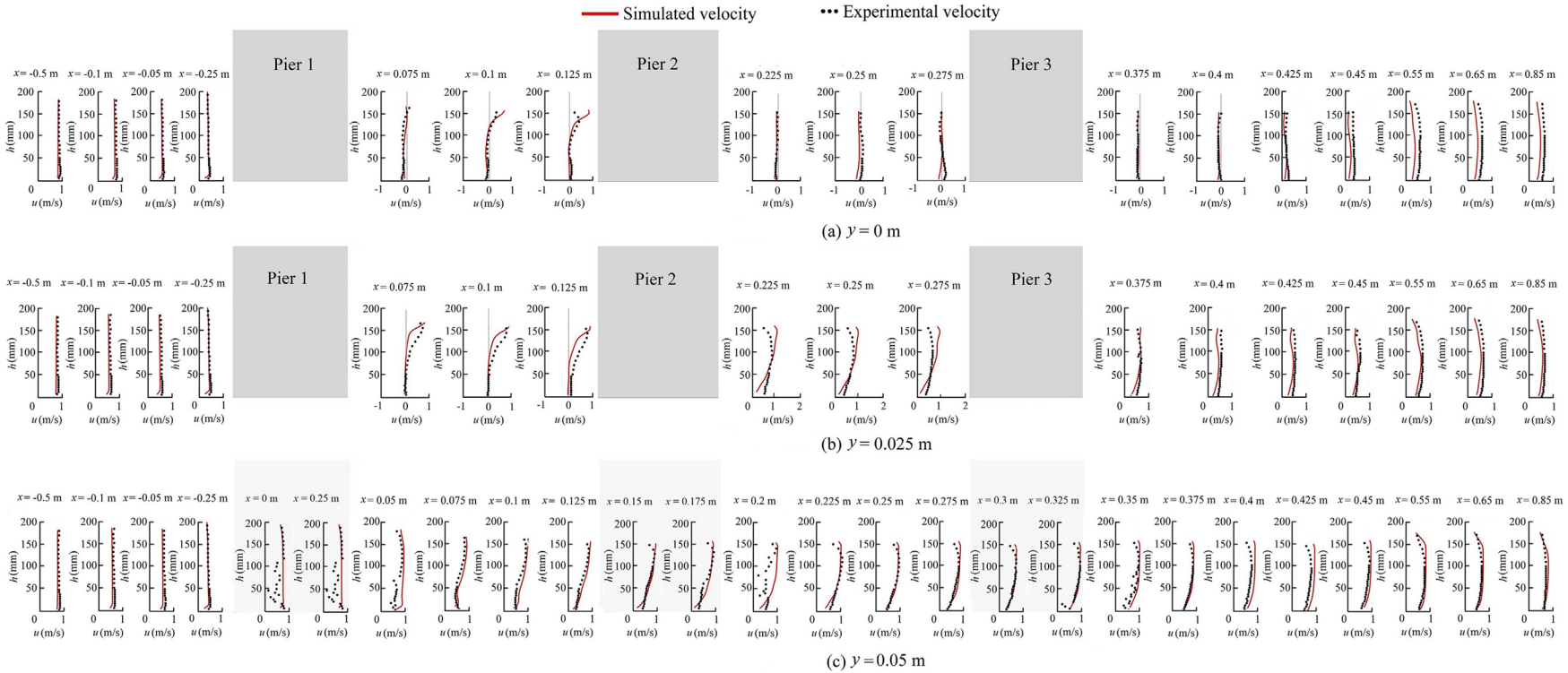

Fig. 12. Numerical and experimental velocity profiles.

dynamics around bridge piers. These observations can inform the development of more practical and simplified field measurement strategies for future research endeavours.

Declaration of competing interest

The authors declare no conflicts of interest.

References

Alemi, M., Pêgo, J.P., Maia, R., 2019. Numerical simulation of the turbulent flow around a complex bridge pier on the scoured bed. Eur. J. Mech. B Fluid 76, 316−331. https://doi.org/10.1016/j.euromechflu.2019.03.011.

Amina, Tanaka, N., 2022. Numerical investigation of 3D flow properties around finite emergent vegetation by using the two-phase volume of fluid (VOF) modeling technique. Fluid 7(5), 175. https://doi.org/10.3390/fluids7050175.

Ataie-Ashtiani, B., Aslani-Kordkandi, A., 2012. Flow field around side-by-side piers with and without a scour hole. Eur. J. Mech. B Fluid 36, 152−166. https://doi.org/10.1016/j.euromechflu.2012.03.007.

Bao, Y., Zhou, D., Huang, C., 2010. Numerical simulation of flow over three circular cylinders in equilateral arrangements at low Reynolds number by a second-order characteristic-based split finite element method. Comput. Fluid 39(5), 882−899. https://doi.org/10.1016/j.compfluid.2010.01.002.

Blanckaert, K., Lemmin, U., 2006. Means of noise reduction in acoustic turbulence measurements. J. Hydraul. Res. 44, 3−17. https://doi.org/10.1080/00221686.2006.9521657.

Breuer, M., 2000. A challenging test case for large eddy simulation: High Reynolds number circular cylinder flow. Int. J. Heat Fluid Flow 21(5), 648−654. https://doi.org/10.1016/S0142-727X(00)00056-4.

Chavan, R., Kumar, B., 2017. Experimental investigation on flow and scour characteristics around tandem piers in sandy channel with downward seepage. J. Mar. Sci. Appl. 16(3), 313−322. https://doi.org/10.1007/s11804-017-1426-6.

Chavan, R., Huai, W., Kumar, B., 2020. Alluvial channel hydrodynamics around tandem piers with downward seepage. Front. Struct. Civ. Eng. 14, 1445−1461. https://doi.org/10.1007/s11709-020-0648-x.

Cheng, Y., Lien, F., Yee, E., Sinclair, R., 2003. A comparison of large eddy simulations with a standard $k-\varepsilon$ Reynolds-averaged Navier−Stokes model for the prediction of a fully developed turbulent flow over a matrix of cubes. J. Wind Eng. Ind. Aerod. 91(11), 1301−1328. https://doi.org/10.1016/j.jweia.2003.08.001.

Dargahi, B., 1989. The turbulent flow field around a circular cylinder. Exp. Fluid 8, 1−12. https://doi.org/10.1007/BF00203058.

Díaz Lozada, J.M., García, C.M., Scacchi, G., Oberg, K.A., 2021. Dynamic selection of exposure time for turbulent flow measurements. J. Hydraul. Eng. 147, 04021035. https://doi.org/10.1061/(ASCE)HY.1943-7900.0001922.

Discetti, S., Coletti, F., 2018. Volumetric velocimetry for fluid flows. Meas. Sci. Technol. 29, 042001. https://doi.org/10.1088/1361-6501/aaa571.

Ferziger, J.H., Perić, M., Street, R.L., 2002. Computational Methods for Fluid Dynamics. Springer, Berlin, Heidelberg.

Ghaderi, A., Abbasi, S., 2019. CFD simulation of local scouring around airfoil-shaped bridge piers with and without collar. Sādhanā 44, 216. https://doi.org/10.1007/s12046-019-1196-8.

Hamidi, A., Siadatmouavi, S.M., 2018. Numerical simulation of scour and flow field for different arrangements of two piers using SSIIM model. Ain Shams Eng. J. 9(4), 2415−2426. https://doi.org/10.1016/j.asej.2017.03.012.

Helmi, A.M., Shehata, A.H., 2021. Three-dimensional numerical investigations of the flow pattern and evolution of the horseshoe vortex at a circular pier during the development of a scour hole. Appl. Sci. 11, 6898.

Hirt, C.W., Nichols, B.D., 1981. Volume of fluid (VOF) method for the dynamics of free boundaries. J. Comput. Phys. 39(1), 201−225. https://doi.org/10.1016/0021-9991(81)90145-5.

Hong, J.H., Chiew, Y.M., Lu, J.Y., Lai, J.S., Lin, Y.B., 2012. Houfeng bridge failure in Taiwan. J. Hydraul. Eng. 138(2), 186−198. https://doi.org/10.1061/(ASCE)HY.1943-7900.0000430.

Hu, P., Yu, M., 2023. Experimental study of secondary flow in narrow and sharp open-channel bends. J. Appl. Fluid Mech. 16, 1767−1777. https://doi.org/10.47176/jafm.16.09.1672.

Huang, W., Yang, Q., Xiao, H., 2009. CFD modeling of scale effects on turbulence flow and scour around bridge piers. Comput. Fluid 38(5), 1050−1058. https://doi.org/10.1016/j.compfluid.2008.01.029.

Ikani, N., Pu, J.H., Taha, T., Hanmaiahgarib, P.R., Penna, N., 2023. Bursting phenomenon created by bridge piers group in open channel flow. Environ. Fluid Mech. 23, 125−140. https://doi.org/10.1007/s10652-023-09910-8.

Ikani, N., Pu, J.H., Zang, S., Al-Qadami, E.H.H., Razi, A., 2024. Detailed turbulent structures investigation around piers group induced flow. Exp. Therm. Fluid Sci. 152, 111112. https://doi.org/10.1016/j.expthermflusci.2023.111112.

Jia, Y., Altinakar, M., Guney, M.S., 2018. Three-dimensional numerical simulations of local scouring around bridge piers. J. Hydraul. Res. 56(3), 351−366. https://doi.org/10.1080/00221686.2017.1356389.

Karim, M.F., Tanimoto, K., Hieu, P.D., 2009. Modelling and simulation of wave transformation in porous structures using VOF based two-phase flow model. Appl. Math. Model. 33(1), 343−360. https://doi.org/10.1016/j.apm.2007.11.016.

Kim, S.E., Choudhury, D., Patel, B., 1999. Computations of complex turbulent flows using the commercial code FLUENT. In: Salas, M.D., Hefner, J.N., Sakell, L. (Eds.), Modeling Complex Turbulent Flows. Springer, Dordrecht, pp. 259−276.

Lade, A.D., Deshpande, V., Kumar, B., Oliveto, G., 2019. On the morphodynamic alterations around bridge piers under the influence of instream mining. Water 11(8), 1676. https://doi.org/10.3390/w11081676.

Li, D., Muste, M., Wang, X., 2007. Quantification of the bias error induced by velocity gradients. Meas. Sci. Technol. 19, 015402. https://doi.org/10.1088/0957-0233/19/1/015402.

Loli, M., Mitoulis, S.A., Tsatsis, A., Manousakis, J., Kourkoulis, R., Zekkos, D., 2022. Flood characterization based on forensic analysis of bridge collapse using UAV reconnaissance and CFD simulations. Sci. Total Environ. 822, 153661. https://doi.org/10.1016/j.scitotenv.2022.153661.

Marian, M., Kim, J., Kim, D., 2021. Impact of the sampling duration on the uncertainty of averaged velocity measurements with acoustic instruments. Hydrol. Process. 35, e14125. https://doi.org/10.1002/hyp.14125.

Melville, B.W., Raudkivi, A.J., 1996. Effects of foundation geometry on bridge pier scour. J. Hydraul. Eng. 122(4), 203−209. https://doi.org/10.1061/(ASCE)0733-9429(1996)122:4(203).

Park, H., Hwang, J.H., 2021. A standard criterion for measuring turbulence quantities using the four-receiver acoustic Doppler velocimetry. Front. Mar. Sci. 8, 681265. https://doi.org/10.3389/fmars.2021.681265.

Pedras, M.H., de Lemos, M.J., 2000. On the definition of turbulent kinetic energy for flow in porous media. Int. Commun. Heat Mass Tran. 27(2), 211−220. https://doi.org/10.1016/S0735-1933(00)00102-0.

Pourshahbaz, H., Abbasi, S., Pandey, M., Pu, J.H., Taghvaei, P., Tofangdar, N., 2022. Morphology and hydrodynamics numerical simulation around groynes. ISH J. Hydraul. Eng. 28(1), 53−61. https://doi.org/10.1080/09715010.2020.1830000.

Prendergast, L.J., Gavin, K., 2014. A review of bridge scour monitoring techniques. J. Rock Mech. Geotech. Eng. 6(2), 138−149. https://doi.org/10.1016/j.jrmge.2014.01.007.

Pu, J.H., Hussan, K., Tait, S.J., 2007. Simulation of turbulent free surface obstructed flow within channels. In: Proceedings of the 32nd IAHR World Congress. IAHR, Venice.

Pu, J.H., Cheng, N.S., Tan, S.K., Shao, S., 2012. Source term treatment of SWEs using surface gradient upwind method. J. Hydraul. Res. 50(2), 145−153. https://doi.org/10.1080/00221686.2011.649838.

Pu, J.H., Shao, S., Huang, Y., 2014. Numerical and experimental turbulence studies on shallow open channel flows. J. Hydro-env. Res. 8(1), 9−19. https://doi.org/10.1016/j.jher.2012.12.001.

Pu, J.H., 2015. Turbulence modelling of shallow water flows using Kolmogorov approach. Comput. Fluid 115, 66−74. https://doi.org/10.1016/j.compfluid.2015.03.010.

Pu, J.H., 2021. Velocity profile and turbulence structure measurement corrections for sediment transport-induced water-worked bed. Fluid 6(2), 86. https://doi.org/10.3390/fluids6020086.

Qi, H., Zheng, J., Zhang, C., 2020. Numerical simulation of velocity field around two columns of tandem piers of the longitudinal bridge. Fluid 5(1), 32. https://doi.org/10.3390/fluids5010032.

Ramamurthy, A., Qu, J., Vo, D., 2005. Volume of fluid model for an open channel flow problem. Can. J. Civ. Eng. 32(5), 996−1001. https://doi.org/10.1139/l05-038.

Salaheldin, T.M., Imran, J., Chaudhry, M.H., 2004. Numerical modeling of three-dimensional flow field around circular piers. J. Hydraul. Eng. 130(2), 91−100. https://doi.org/10.1061/(ASCE)0733-9429(2004)130:2(91).

Song, T., Chiew, Y., 2001. Turbulence measurement in nonuniform open-channel flow using acoustic Doppler velocimeter (ADV). J. Eng. Mech. 127, 219−232. https://doi.org/10.1061/(ASCE)0733-9399(2001)127:3(219).

Soori, S., Karami, H., 2024. Laboratory study on relative energy loss and backwater rise at bridge piers and abutment. Model. Earth Syst. Env. 10, 1359−1373. https://doi.org/10.1007/s40808-023-01830-2.

Voulgaris, G., Trowbridge, J.H., 1998. Evaluation of the acoustic Doppler velocimeter (ADV) for turbulence measurements. J. Atmos. Ocean. Technol. 15, 272−289. https://doi.org/10.1175/1520-0426(1998)015<0272:EOTADV>2.0.CO;2.

Yang, Y., Xiong, X., Melville, B.W., Sturm, T.W., 2021. Dynamic morphology in a bridge-contracted compound channel during extreme floods: Effects of abutments, bed-forms and scour countermeasures. J. Hydrol. 594, 125930. https://doi.org/10.1016/j.jhydrol.2020.125930.

Zaid, M., Yazdanfar, Z., Chowdhury, H., Alam, F., 2019. Numerical modeling of flow around a pier mounted in a flat and fixed bed. Energy Proc. 160, 51−59. https://doi.org/10.1016/j.egypro.2019.02.118.